Spatially resolved scanning tunneling spectroscopy of single-layer steps on Si(100) surfaces

Xiqiao Wang,[1,2] Pradeep Namboodiri,[2] Kai Li,[2] Xiao Deng,[2,3] and Richard Silver[2]
[1]*Chemical Physics Program, University of Maryland, College Park, Maryland 20742, USA*
[2]*National Institute of Standards and Technology, 100 Bureau Dr., Gaithersburg, Maryland 20899, USA*
[3]*School of Physics Science and Engineering, Tongji University, Shanghai 200092, China*
(Received 19 July 2016; revised manuscript received 17 August 2016; published 8 September 2016)

Single-layer steps at Si(100) surfaces/interfaces present significant challenges to the quantitative characterization of buried dopant devices as well as the accurate imaging and relocation of fabricated quantum structures. We demonstrate the detailed spatially resolved scanning tunneling spectroscopy study across monolayer step edges on Si(100) surfaces and quantitative determination of the local density of state distributions and behavior of the band gap at step edges. The influence on the local electrostatic environment due to step edge states has been quantified while accounting for the effects of scanning tunneling measurement conditions. The dangling bond states on Si(100) surfaces are utilized as a fingerprint to quantify the local band bending landscape and to make corrections to the experimentally observed surface state energy levels and band gap values at the step edge regions. We observe a significant band gap narrowing behavior along a rebonded single-layer type B step edge on a degenerately boron-doped p-type Si substrate.

DOI: 10.1103/PhysRevB.94.125306

I. INTRODUCTION

Defects on surfaces can significantly affect surface electronic properties. Understanding the electronic and geometric effects that result from surface defects is critical to meaningful scanning tunneling microscopy (STM) characterization of donor-based atomic-scale quantum devices, particularly those fabricated using hydrogen lithography [1,2]. Although defects on flat terraces can be largely eliminated by careful sample cleaning and optimization of vacuum thermal processes, step edge defects are inherent to Si(100) surfaces. The driving force behind the step formation on Si(100) surfaces is to minimize the anisotropic surface strain energy induced by the [110] direction miscut angle [3,4]. The step density can further increase after Si homoepitaxial deposition [5], which is an integral part of the donor-based atomic-scale device fabrication process. These effects that result from a large number of step edges can, however, be reduced by creating large atomically flat terraces by controlling the formation of the atomic step/terrace morphology [6]. STM studies [7] have indicated that some step edge formations are active sites to trap and bond Si monomers during Si homoepitaxy growth. It has been shown that atomic steps at a quantum-well interface in a Si-SiGe heterostructure can suppress the valley splitting [8]. Step edges on surfaces have also been proposed as templates for conducting channels and spin chains for future silicon quantum computing [9,10]. Therefore, detailed studies of the electronic properties of single-layer steps on the Si(100) surface not only contribute to successful fabrication and characterization of donor-based atomic-scale quantum devices and provide a better understanding of atomic dynamics on Si(100) surfaces, but also provide a means to engineer the electronic properties of nearby atomic structures.

STM is a powerful tool to investigate the geometric and electronic properties of Si(100) surfaces with atomic resolution. Single-layer step morphology and growth mechanisms on Si(100) surfaces have been intensively studied using STM [4,7,11–22]. In addition, extensive scanning tunneling spectroscopy observations [23–25] and *ab initio* calculations [26–30] have been carried out to study isolated dangling bonds and dangling bond wire systems on H-terminated Si(100) surfaces due to their technological importance as atomic-scale nanowires [31] and potential use in achieving atomic-scale quantum devices [32]. However, in spite of the significant effect on local electronic behavior, there has been very limited experimental [22,33] and theoretical work [3,34] providing insight into the electronic properties of single-layer step edges on the Si(100) surface. In contrast to single point scanning tunneling spectroscopy [22,33], spatially resolved scanning tunneling spectroscopy can provide direct information on the spatial variation of energy states along a line scan.

Single-layer steps on Si(100) surfaces have been intensively studied using STM imaging because of their technical role in the homoepitaxy of Si on Si(100) substrates as well as the heteroepitaxy of III-V semiconductors on Si(100) substrates [35–37]. Single-layer steps on Si(100) surfaces can be classified as single-layer type A (SA) steps and single-layer type B (SB) steps [38], where the dimer is perpendicular to the step edge on the upper terrace of an SA step, and parallel to the step edge on the upper terrace of an SB step as shown in Fig. 1.

In this paper, we present a spatially resolved scanning tunneling spectroscopy (STS) study across single-layer SA and SB step edges on Si(100) surfaces at room temperature. On a heavily boron-doped p-type substrate, the local density of states (LDOS) across SA steps was found to be very similar to those observed on flat terraces. STS observations show a narrow surface band gap at the SB step edge with a prominent density of states (DOS) peak located at the lower edge of the unoccupied dangling bond surface states on a clean Si(100)2 $\times$ 1 surface. In order to quantitatively characterize the surface DOS at the step edges as well as their influence on the local electrostatic environment, we employ three-dimensional (3D) electrostatic simulations to first assume a hyperbolic tip shape and fit the tip geometry and work function parameters by comparing the simulated band bending with the experimental

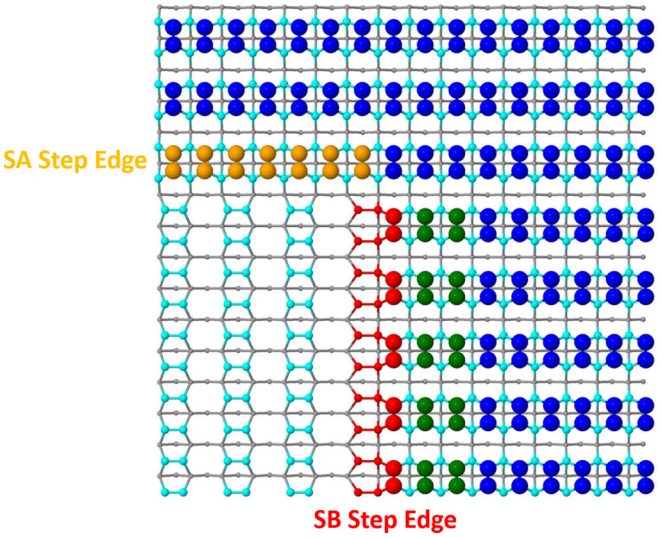

FIG. 1. Atomic structure of the monolayer SA step edge and rebonded SB step edge configurations on Si(100) surfaces as proposed by Chadi [38]. The large spheres represent Si atoms at the upper terrace. The medium spheres represent Si atoms one monolayer below the upper terrace. The light-gray spheres represent the Si atoms of the substrate. Dimers on the upper terrace are perpendicular to the SA step edge and parallel to the SB step edge. The orange spheres represent buckled dimer atoms along the SA step edge. The red spheres represent Si atoms at the rebonded SB step edge. The green spheres represent Si atoms adjacent to the SB step edge on the upper terrace.

values on flat terraces. Then, by estimating the SB edge DOS peak area and width, and their spatial distribution from the STS and STM observations, we fit the edge state energy levels at and near the SB step edge. The simulated local band bending landscape in the proximity of the tip and the SB step edge at various sample bias conditions are compared with the features in a measured spectroscopy map. Finally, the observed surface band gap at the SB step edge is corrected using the simulated local band bending results.

II. EXPERIMENTAL METHOD

A degenerately boron-doped p-type Si(100) substrate (0.01–0.02 Ω cm miscut angle $<\pm 0.25°$) was sonicated in deionized water and isopropanol at room temperature followed by chemical cleaning using RCA and Base Piranha followed by a dip into 2% HF solution before loading into the ultrahigh vacuum system. The substrate was degassed at 550 °C overnight followed by several rapid flash anneals to 1200 °C using direct current heating while maintaining the chamber pressure below 9×10^{-10} Torr (1.2×10^{-7} Pa). After the final flash, the substrate was quenched to about 900 °C and slowly cooled down at −2 °C/s to room temperature [39]. Quadrupole high depth resolution second ion mass spectroscopy (SIMS) measurement was used to provide subsurface and bulk dopant density information for experimental and theoretical analyses, which shows that the thermal process results in a subsurface dopant depletion region (due to dopant out-diffusion) extending approximately 30 nm into the substrate. But, because the dopant depletion region

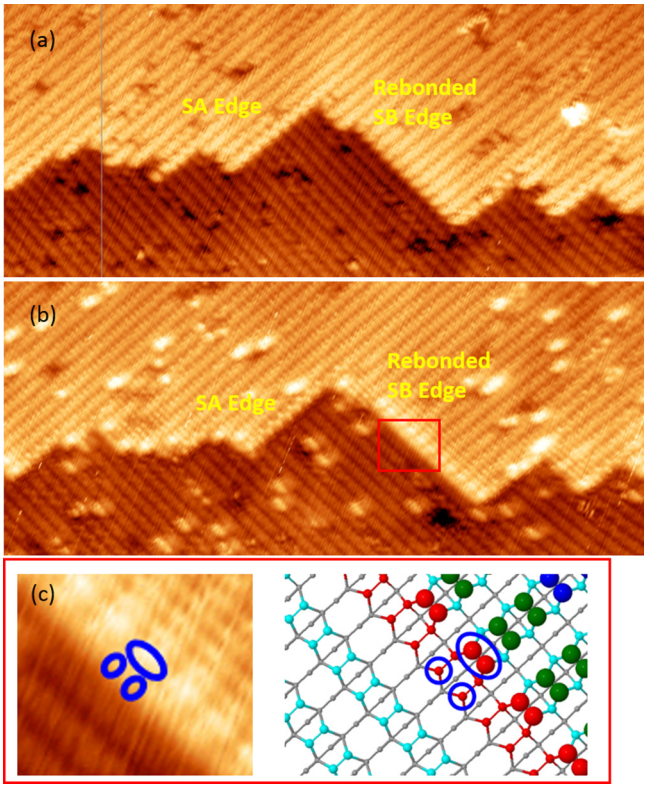

FIG. 2. STM images of single-layer SA and rebonded SB steps on a degenerately boron-doped p-type Si(100) substrate surface. (a) Filled state image: −1.5 V, 0.15 nA. (b) Empty state image: +0.7 V, 0.15 nA. The dimer rows appear as bright rows in the filled state image (a), and appear as dark rows in the empty state image (b). The dimers along SA step edges are buckled. The spatial distribution of unoccupied edge states at the rebonded SB step edge is emphasized by the bright protrusions along the rebonded SB step edge in (b). (c) A zoom-in on the squared area in (b) with a close-up view of the corresponding atomic structure, where the large blue circle marks a dimer at the upper edge of the rebonded SB step edge, and the two small circles mark the unpaired dangling bonds at the lower edge of the rebonded SB step edge.

is still degenerately doped after sample flashing, we treat this dopant depletion effect as negligible. Therefore, in this work, we assume a uniform dopant density as measured from deep inside the bulk sample substrate ($3.5 \times 10^{18}/\text{cm}^3$). A chemically etched polycrystalline tungsten tip was cleaned *in situ* by annealing to approximately 1000 °C for several hours before use. Tip condition was monitored by STM imaging stability as well as robust atomic resolution imaging of Si(100) dimers.

STM images at both negative and positive sample biases were taken on step edges, as shown in Fig. 2. The dimer rows appear as bright rows in the filled state STM image in Fig. 2(a), and appear as dark rows in the empty state STM image in Fig. 2(b). To map the LDOS of the surface, we took I-V curves at points every 0.2 nm along the STS lines as depicted in the STM images in Figs. 3(b) and 3(c). The spectroscopy line in Fig. 3(b) was taken across dimers on a flat terrace. The spectroscopy line in Fig. 3(c) intersects an SA step edge and an eight-dimer-row–wide (∼6.16 nm wide) rebonded SB step

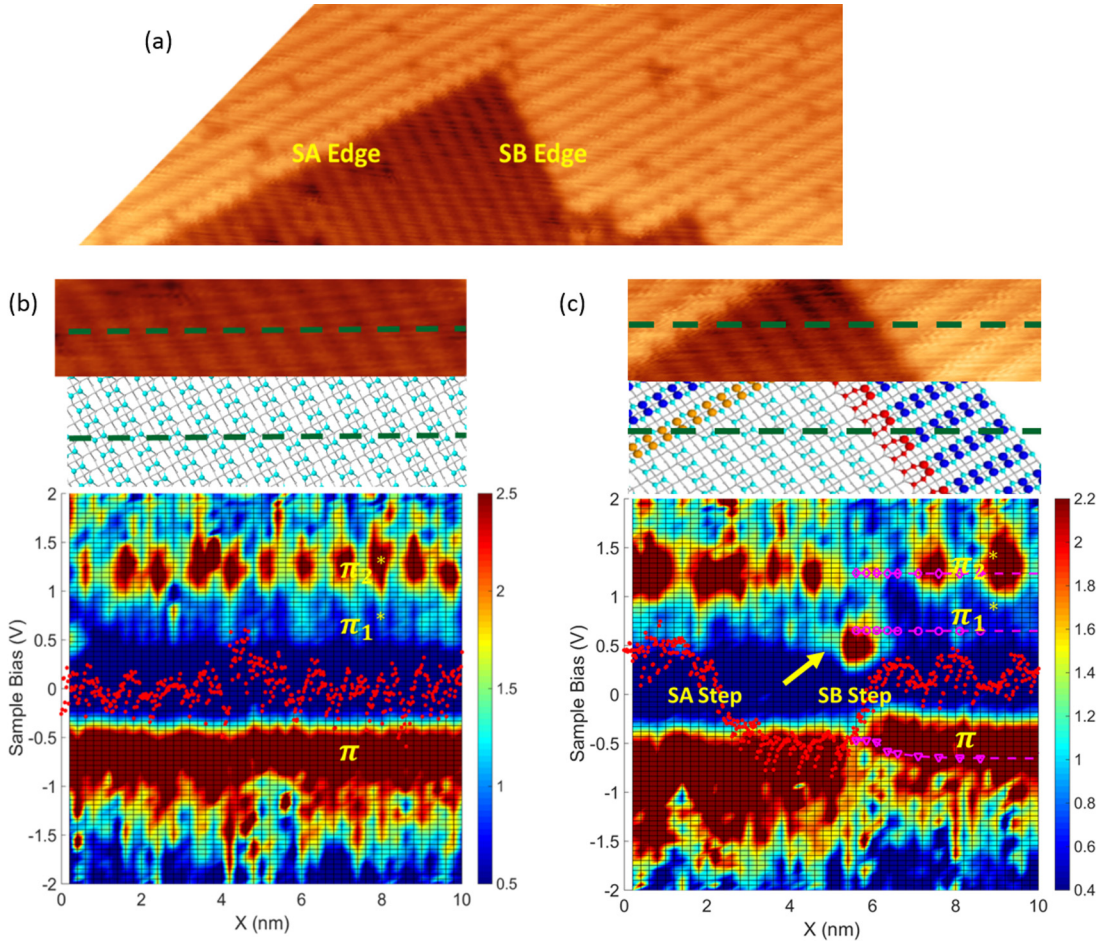

FIG. 3. (a) A filled state STM image of an SA and a rebonded SB step edge taken at −1.8 V, 0.18 nA. (b) plots the $(dI/dV)/\overline{(I/V)}$ spectra across dimer rows on a flat terrace. (b) plots the $(dI/dV)/\overline{(I/V)}$ spectra across a monolayer SA step edge and a rebonded SB step edge. The spectroscopy paths are indicated by the dashed lines in the STM images and the atomic structure diagrams above the spectroscopy maps. The $(dI/dV)/\overline{(I/V)}$ spectra are plotted in color scales [in arbitrary units (a.u.)] with the bias voltage on the vertical axes and the spatial coordinate X on the horizontal axes. The red dots in the spectroscopy maps illustrate the measured topography profiles along the spectroscopy paths in arbitrary units. The spectroscopic features from the π, π_1^*, and π_2^* surface dangling bond states are marked in yellow, as will be discussed in the experimental section. The yellow arrows in (c) emphasize the prominent unoccupied LDOS peak at the rebonded SB step edge as well as a measured peak position shift along the spectroscopy path. The dashed lines in red-violet represent the simulated local band bending curves under the tip apex, as will be discussed in the theoretical section.

edge at the same time. The section was taken about 30° with respect to the upper terrace dimer row direction. The *I-V* curves at each spatial point were measured at a constant tip-sample separation, which was set by the constant current imaging condition $V = -1.8\,\mathrm{V}$, and $I = 0.18\,\mathrm{nA}$, with the feedback loop off. The normalized differential conductance (dn) spectra, $(dI/dV)/\overline{(I/V)}$, were numerically derived from the measured *I-V* spectra following Feenstra [40,41]. The tunneling current contains an energy integral of the product of the LDOS $\rho(E)$ and transmission probability, $T(E,eV)$, as shown in Eq. (2.1), where E is the DOS energy level relative to the sample Fermi level and V is the sample bias. The normalized differential conductance $(dI/dV)/(I/V)$ can be expressed in the form of Eq. (2.2). Since $T(E,eV)$ and $T(eV,eV)$ appear as ratios in both the denominator and numerator, the transmission coefficient's exponential dependence on the tip-sample separation and sample bias voltage tends to cancel. As a result, the normalization procedure essentially eliminates the dependence of the measured DOS features at different tip-sample separations. The second term in the numerator in Eq. (2.2) is a slowly varying "background" term due to the dependence on the sample bias voltage of the tails of the local wave functions in the tunneling barrier [41]. The total conductance (I/V) in the denominator in Eq. (2.2) is a normalization factor. In order to avoid divergence of the dn spectrum at the band edges of large-band-gap surfaces and to obtain an experimental approximation of the surface DOS, the conductance (I/V) is smoothed over the range of voltages, denoted as $\overline{(I/V)}$, following Feenstra [40]. ΔV is the band gap of bulk silicon, $\exp(-a'|V|)$ is a weighting factor, and a' is a typical exponential slope value, $2\,\mathrm{V}^{-1}$, of the tunneling current $I(V)$ [40]. In summary, the d_n spectra as a function of sample bias approximately represent the surface LDOS distribution at different energy levels ($\mathrm{cm}^{-2}\ \mathrm{eV}^{-1}$). To first order, the integrated area under each peak is proportional to the total LDOS (cm^{-2}) of the corresponding surface

TABLE I. Surface dangling bond state parameters on flat terraces of Si(100) surfaces adopted from previous PES and DFT results [42–50,53,54]. In the intrinsic edge state model, which is to be discussed in the theoretical section, the surface state density and FWHM at the step edge are scaled by the same factors used when scaling the peaks from the flat terraces. E_1 and E_2 are the two fitting parameters in the intrinsic SB edge state model.

Dangling bond states		Donorlike π bands			Acceptorlike π^* bands		
		Energy level above VBM (eV)	Surface density ($/cm^2$)	FWHM (eV)	Energy level above VBM (eV)	Surface Density ($/cm^2$)	FWHM (eV)
On flat terraces	First subband	−0.50	3.37×10^{14}	0.30	0.69	3.37×10^{14}	0.30
	Second subband	−0.25	3.37×10^{14}	0.20	1.20	3.37×10^{14}	0.20
At SB step edge	SB edge state peaks (intrinsic model)	E_1	4.20×10^{14}	0.32	E_2	8.11×10^{14}	0.30

state.

$$I \propto \int_0^{eV} \rho(E)T(E,eV)dE, \tag{2.1}$$

$$\frac{dI/dV}{I/V} = \frac{\rho(eV) + \int_0^{eV} \frac{\rho(E)}{T(eV,eV)} \frac{d}{d(eV)}[T(E,eV)]dE}{\frac{1}{eV}\int_0^{eV} \rho(eV)\frac{T(E,eV)}{T(eV,eV)}dE}, \tag{2.2}$$

$$\overline{(I/V)} = \exp(a'|V|) \int_{-\infty}^{+\infty} [I(V')/V'] \times \exp\left\{\frac{-|V'-V|}{\Delta V}\right\} \exp(-a'|V'|)dV'. \tag{2.3}$$

III. EXPERIMENTAL RESULTS AND DISCUSSION

A. Identifying surface dangling bond states in scanning tunneling spectroscopy

The electronic structure of Si(100) surfaces has been extensively studied using angle-resolved photoemission spectroscopy [42–47], inverse photoemission [44,48], electron-energy-loss spectroscopy, two-photon photoemission spectroscopy [49,50], as well as scanning tunneling spectroscopy [51,52] and numerous theoretical calculations [53,54]. The asymmetric (buckled) $c(4 \times 2)$ dimer model of the Si(100) surfaces, first introduced by Chadi [55], results in minimum surface free energy and a semiconducting surface band gap that agrees with photoemission experiments. This $c(4 \times 2)$ buckled dimer reconstruction structure is well known as the ground state of the Si(100) surface at low temperature. The asymmetric dimer atoms are connected by a dimer bond and are attached to the bulk substrate via back bonds. The occupied dangling bond state is primarily located at the upper Si atom of the buckled dimer, and the unoccupied dangling bond state is primarily located at the lower dimer atom. They are conventionally denoted as the D_{up} and D_{down} dangling bond states. Since the charge transfer from the lower dimer atom to the upper atom is incomplete [51], and also because of the fact that STM/STS observations at room temperature are the result of time-averaged rapid flipping of buckled dimers, we adopted the nomenclature of π and π^* (anti-π) states from a symmetric dimer picture to represent the occupied and unoccupied dangling bond states for the remainder of this paper. The agreement between room temperature photoemission spectroscopy results with low-temperature electronic structure calculations suggests that the energetics of buckled dimer surface reconstruction persists up to room temperature [56].

We follow the conventional description and denote the two occupied π surface bands as π_1 and π_2, and the two unoccupied π^* surface bands as π_1^* and π_2^*, which are derived from the four dangling bonds in each of the $c(4 \times 2)$ unit cells [43,44,47,56–58]. Based on previous photoemission experiments [47,48,59–62] and theoretical results [52,62–64] on the π and π^* band structures on Si(100) surfaces, we adopted the following set of surface dangling bond parameters in Gaussian distribution in this study [Table I and Fig. 6(b)]. The π band is composed of two subbands centered at −0.25 and −0.50 eV below the valence band maximum (VBM) with FWHM of 0.30 and 0.20 eV, respectively. The two π^* subbands are centered at 0.69 eV (averaged between experimental values of 0.66 eV [48] and 0.72 eV [47]) and 1.20 eV above the VBM with FWHM of 0.30 and 0.20 eV, respectively. From the atomic density on the Si(100) plane, we have $3.37 \times 10^{14}/cm^2$ as the surface state density for each of the four dangling bond states (π_1, π_2, π_1^*, and π_2^*), including spin degeneracy.

Photoemission spectroscopy (PES) studies [59,65–67] have shown that the Si(100) surface is semiconducting at room temperature. The surface band gap of the clean Si(100) surface is approximately half the band gap of an H-terminated Si(100) surface [58]. Due to the inelastic scattering of vertically injected tunneling electrons from a 3D tip at the surface, the measured DOS spectrum is an integral over the entire two-dimensional (2D) k-space band diagram. At room temperature, we obtained dn curves on both clean and H-terminated Si(100) surfaces, as shown by the brown and blue curves in Fig. 4(b), that agree very well with previous studies [24,51,52,58,60,68]. The absence of the three peaks on the hydrogen-terminated surface confirms that the occupied state peak and the two unoccupied state peaks on clean Si(100) surfaces result from the dangling bond surface states. On clean Si(100) surfaces, the peak in the negative bias region arises from the occupied π_2 band centered at 0.25 eV below the VBM. The occupied π_1 band cannot be resolved due to its broad dispersion in k space and the limited energy resolution at room temperature. The first unoccupied state peak arises from the states at the bottom of the unoccupied surface π^* band centered at 0.69 eV above the VBM. The assignment of the second unoccupied state peak

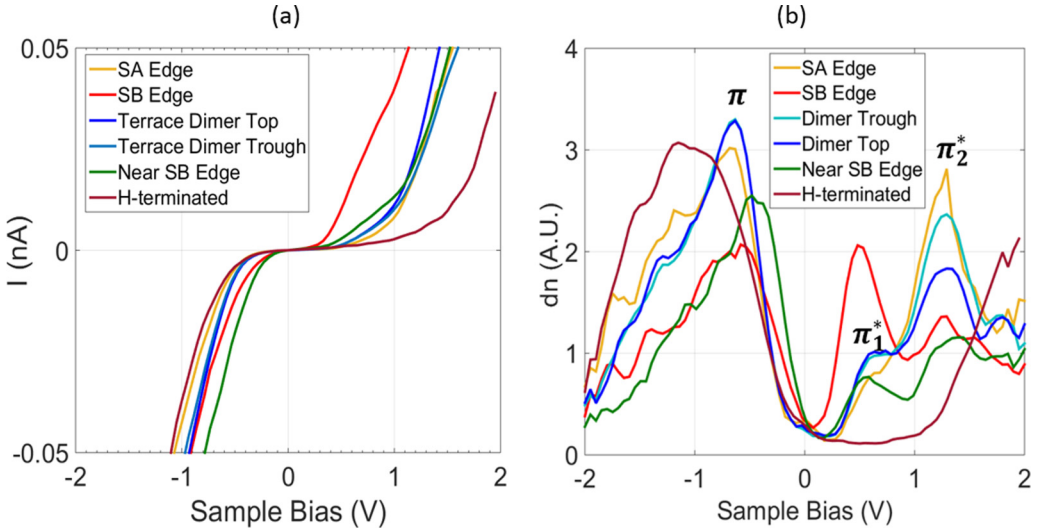

FIG. 4. (a) The averaged I-V curve spectra, and (b) the normalized differential conductance $(dI/dV)/\overline{(I/V)}$ spectra (dn spectra) measured at dimer tops and dimer troughs on flat terraces as well as at monolayer step edge regions on a clean Si(100)2 × 1 surface of a $3.5 \times 10^{18}/\text{cm}^3$ boron-doped p-type substrate. The spectrum curves measured on the flat terraces of a hydrogen-terminated Si(100)2 × 1 surface of the same substrate are also plotted for comparison. The zero sample bias aligns with the substrate's Fermi level. Band gap features appear in all the spectroscopy curves, indicating that the monolayer step edges under observation do not change the semiconducting nature of the surface, but do change the local semiconducting properties of the surface.

has been discussed extensively [51,52,58,60,61] regarding whether this peak originates from unoccupied backbond states or from the upper edge of the π^* band. The second unoccupied state peaks in the blue and cyan curves in Fig. 4(b) show a spatial variation with a high intensity between dimer rows and a low intensity over the dimer rows, which agrees with recent experimental [60] and theoretical [63] studies. Previous interpretation [25,53,64,69] assigned this peak to either the unoccupied backbond* states or the unoccupied dimer-bond states, while the dangling bond π^* state might also mix into this peak [63]. However, due to the high strength of the second unoccupied state peak in the dn spectrum and the relatively high energy level of the unoccupied dimer-bond state from photoemission results [44,49,50], most recent STS observations and *ab initio* calculations [51,52] have assigned this second unoccupied state peak to the upper edge of the π^* dangling bond state band (π_2^* state band). The unoccupied dimer-bond state may account for the third unoccupied state peak as observed near the +2.0 V sample bias voltage [51]. In summary, we assign the observed first occupied state peak in our STS spectra to the second occupied π band (π_2 band) at −0.25 eV below the VBM, and the observed first and second unoccupied state peaks to the π_1^* and π_2^* bands at +0.69 and +1.20 eV above the VBM, respectively.

The measured I-V curves are averaged over different regions (as indicated in Fig. 1) on the surface and converted to dn spectra as shown in Figs. 4(a) and 4(b). The SB edge region is defined by the bright protrusion area, about 0.8 nm wide, along the SB step edge, as shown in Figs. 2(b) and 2(c). The SA step edge region is about one dimer row wide along the SA step edge. The "near SB edge region" covers the upper terrace areas within two to three dimers of the SB edge (the green region in Fig. 1). The flat terrace region is defined as areas at least 4 nm away from any step edge. While the surface dangling bond states that correspond to π, π_1^*, and π_2^* bands are recognizable near the SB step edge, the measured dangling bond peak positions near the SB step edge feel strong Coulomb interactions from the charge states at the edge, and therefore shift from the corresponding peak positions as observed on flat terraces. As the data acquisition points move further away from the SB step edge into the upper flat terrace, the measured spectroscopic features approach the blue curve in Fig. 4(b) that was obtained on a flat terrace. Due to the finite size of the tip, the LDOS measurements on a lower terrace near a step edge are expected to strongly convolute with the step edge geometry. The potential irregularity of the tip shape could further complicate this geometric convolution effect. In the interest of simplicity, we only used the LDOS spectra measured on the upper terrace side of the step edge where the geometrical convolution with the step edge is relatively small.

The room temperature measured dn peaks from dangling bond states are fitted using a Gaussian function, as shown in Fig. 5. The area under each of the dangling bond peaks is averaged over dimer tops and dimer troughs on flat terraces and then normalized to the known dangling bond DOS values on flat terraces, $3.37 \times 10^{14}/\text{cm}^2$. The surface LDOS at the step edges are scaled by the same factors used when scaling the peaks from the flat terraces. The derived LDOS values are summarized in Table II. Comparing the DOS values on flat terraces with those at an SA step edge, the densities of the π_2 and π_1^* dangling bond states are lower and the densities of the π_1 and π_2^* dangling bond states are higher. But the total number of dangling bond states at the SA step edge is roughly conserved. The upper terrace near the SB step edge has fewer dangling bond states in total, and the SB step edge has larger dangling bond DOS in total as compared with the total dangling bond DOS on the flat terrace. However, the total number of dangling bond states is roughly conserved in combining "near SB step edge" and the SB step edge regions.

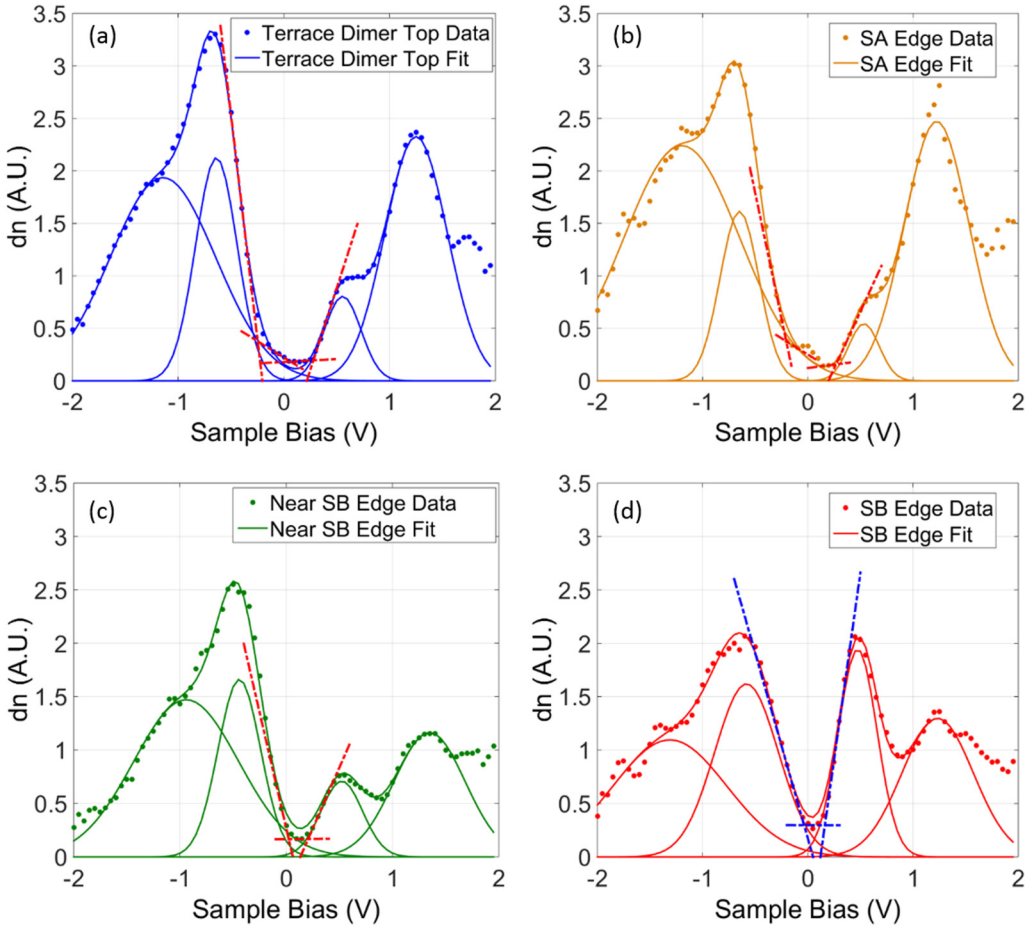

FIG. 5. The measured surface states peaks in the $(dI/dV)/\overline{(I/V)}$ spectra curves are fitted using Gaussian distributions. (a), (b), (c), and (d) plot the original spectra data points as well as the fitted curves on flat terraces, at the SA step edge, near the SB step edge, and at the SB step edge, respectively. The four peaks on the flat terrace correspond to the π_1, π_2, π_1^*, and π_2^* dangling bond states. The observed onset energy levels of the band extrema are determined by assuming linear onsets on the normalized differential conductance spectra following Feenstra [40]. The spectra are fitted with straight lines on either side of the onset, and the onset position is obtained by the intersection of the lines.

B. Tunneling spectra at the single-layer SA step edge

Yokoyama *et al.* [62] has studied the influence of step induced local stress on dimer buckling and reconstruction phase transitions on Si(100) surfaces. At room temperature, the buckling along the upper edge of an SA step is stabilized due to an increased flip-flop barrier height caused by a small displacement (lattice strain) of second layer atoms in the presence of an SA step edge [3,19]. The dimer rows are buckled along the upper edge of SA steps in our STM images [as shown in Figs. 2(a), 2(b), and 3(a)], which agrees with the previous observations [12,13,57] at room temperature.

SA step edges have a lower formation energy than SB step edges because SA step edges do not lead to large lattice strains or extra dangling bonds. The surface dimerization

TABLE II. Normalized DOS of each surface state peak at different areas on the Si(100) surface. The area under each of the dangling bond peaks is averaged over dimer tops and dimer troughs on flat terraces and then normalized to the known dangling bond DOS values. The surface LDOS at the step edges are scaled by the same factors used when scaling the peaks from the flat terraces.

	DOS peaks normalized to the average of dimer top and trough ($\times 10^{14}$/cm^2)				
Surface regions	First occupied state peak	Second occupied state peak	First unoccupied state peak	Second unoccupied state peak	Total
Terrace ave.	3.37	3.37	3.37	3.37	13.48
Dimer top	3.29	3.59	3.13	3.72	13.73
Dimer trough	3.45	3.15	3.61	3.02	13.23
SA edge	4.20	2.56	1.79	4.10	12.65
Near SB edge	2.47	2.86	3.12	2.11	10.56
SB edge	2.01	4.20	8.11	2.38	16.70

is nearly unchanged near an SA step edge [38,70]. Along the upper edge of an SA step, only one buckling type was observed experimentally, where the upper atoms in the buckled dimers are aligned with the lower terrace dimer centers, and the lower atoms in the buckled dimer are aligned with the troughs between dimer rows on the lower terrace [13,19]. The appearance of alternative buckling along the first dimer row on the upper terrace of an SA step has been shown to be induced by step edge geometries rather than electronic structure [3]. Our dn spectra at an SA step edge [yellow curve in Fig. 4(b)] reveals that its electronic structure behaves very similarly to that on flat terraces, which supports previous observations. A band gap of about 0.5 eV observed at an SA step edge is roughly the same as that observed on flat terraces. In addition, the continuity of the dn spectra across the SA step edge [Fig. 3(c)] shows that the presence of an SA step edge introduces little perturbation to the local electronic environment.

C. Tunneling spectra at the single-layer SB step edge

The observed monolayer SB step edges in this work appear bright in low positive sample bias imaging conditions as shown in Figs. 2(b) and 2(c). As can be seen from the red curve in Fig. 4(b), at the SB step edge, a prominent unoccupied state peak stands out near the lower edge of the π_1^* surface band. In addition, as the data acquisition point approaches the SB step edge from the upper flat terrace, the observed π state peak shifts towards the higher sample bias voltage as can be seen in Fig. 3(c). The explanation of this peak position shift over space will be given in the theoretical section.

Two types of SB step edge configurations have been proposed by Chadi [38]. One is the nonrebonded SB step edge that does not form dimer bonds with the lower terrace atoms and has a dangling bond on each of the upper terrace edge atoms. The other one is a rebonded SB step edge (as shown in Fig. 1) that forms dimerlike bonds with the lower terrace atoms and has an unpaired dangling bond at each of the Si atoms on the lower terrace edge. The nonrebonded SB step configuration is considered to be energetically unfavorable when compared with the rebonded type SB step edge configuration [13,14,38,71], although the step edge energetics are affected by detailed reconstruction on the upper and lower terraces [3]. In practice, three types of SB step edges have been observed by STM, namely, rebonded SB edges, nonrebonded SB edges, and nonrebonded SB edges with a split-off dimer [13,14,21,22]. As shown by STM imaging in Fig. 2, both the SB step edge dimers on the upper terrace and the edge atoms on the lower terrace appear as bright protrusions in an empty state image [Figs. 2(b) and 2(c)], indicating that the observed SB step edges in this work are rebonded SB step edges [22,72]. The spatial extension of the bright protrusion areas along the rebounded SB step edge in Figs. 2(b) and 2(c) agree very well with the spatial distribution of the prominent unoccupied LDOS peak at the SB step edge, as marked by a yellow arrow in Fig. 3(c). Upon hydrogen chemisorption, the nonrebonded SB step edge becomes energetically favorable and dominates the monolayer SB step structures on hydrogen-terminated Si(100) surfaces [73–75]. We did not observe band gap edge states or local charging effects across either SA or SB step edges on hydrogen-terminated Si(100) surfaces, and the STS spectra across both the SA and SB step edges are essentially the same as the brown curve shown in Fig. 4. This provides additional evidence that the observed edge states on the clean Si(100) surfaces are related to the surface dangling bonds at the step edges.

According to Jaloviar *et al.* [70], the rebonded dimer on the lower terrace has one of its dangling bonds bonded as a backbond with the upper edge atom, and this rebonding causes strain on the backbond of the nearest dimer on the upper terrace. As a result, our observation of the strong enhancement of local density of unoccupied states along the rebonded SB step edge is likely to originate from a combined effect of both the $3p_z$ orbital of the unpaired dangling bond along the lower edge and the rehybridization of rebonded step edge atomic orbitals. Surface atom core level shifts have been used as a tool to probe the local chemical bonding environment of individual surface atoms due to their sensitivity to the local valence charge distributions [76–79]. On clean Si(100) $c(4 \times 2)$ reconstruction surfaces, shifted core components in the surface Si $2p$ spectrum have been identified by previous photoemission spectroscopy and theoretical studies [76–78]. Our characterization of the local valence states and charge redistributions at the rebonded SB step edge may provide additional information on unidentified core shift components.

IV. QUANTIFYING STEP EDGE EFFECTS ON THE LOCAL ELECTROSTATIC ENVIRONMENT

We used band bending calculations to simulate the SB step edge's influence on the local electrostatic environment under various scanning tunneling conditions. The principle underlying the surface band bending calculations can be explained in the following way. The truncation of 3D bulk Si introduces 2D surface states on the surface. The surface charge states give rise to subsurface band bending near the surface. Similarly, the truncation of a 2D flat surface terrace at a step edge introduces one-dimensional (1D) edge states along the step edge. The step edge charge states can give rise to 2D surface band bending. However, since the tunnel junction in an STS measurement has 3D characteristics and the 2D terraces on the Si(100) surface are also sitting on a 3D bulk Si substrate, both the surface charge states and the step edge charge states influence the band bending near a surface step edge.

An example of a band diagram at a specific sample bias is illustrated in Fig. 6(c). The surface band bending is the potential difference between the surface and deep inside the bulk substrate. The STS measured dangling bond energy levels can be expressed as $E_{\mathrm{STS}} = eV_{\mathrm{bias}} + E_{\mathrm{Fermi}}$ above the bulk VBM, where V_{bias} is the corresponding sample bias value at the measured DOS peak. The photoemission spectroscopy results are given by E_{PES} above the VBM. Therefore, the surface band bending E_{BB} canbe derived from the following expression:

$$E_{BB\_i} = E_{\mathrm{STS}\_i} + E_{\mathrm{Fermi}} - E_{\mathrm{PES}\_i}, \tag{4.1}$$

where i stands for π, π_1^*, and π_2^* surface states as observed in the STS spectra. E_{Fermi} is the Fermi level relative to the bulk VBM (0.0246 eV from our semiclassical calculations for this work) and E_{BB} is the band bending value at the sample bias, V_{bias}. Following Eq. (4.1), the experimentally observed local band bending values on the flat terrace and near the SB step

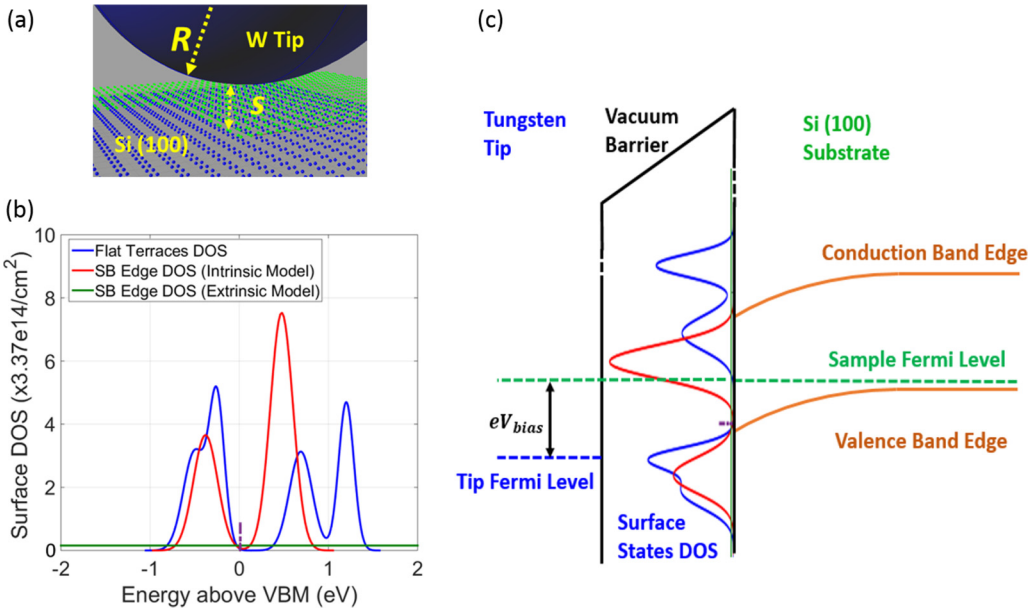

FIG. 6. (a) A 3D diagram showing a hyperbolic tungsten tip at monolayer step edges on a Si(100) surface. s is the tip-sample separation, and R is the tip radius of curvature. (b) The DOS distributions used in band bending simulations. The blue curve represents the occupied and unoccupied dangling bond DOS distributions on flat terraces as adopted from previous PES and DFT results [42–50,53,54]. The red curve represents the best-fit rebonded SB edge DOS distribution using an intrinsic edge DOS model. The flat green line represents the best-fit rebonded SB edge DOS distribution using an extrinsic edge DOS model where a uniform defect state distribution in units of $(\text{cm}^2\,\text{eV})^{-1}$ and an edge state charge neutrality level above the VBM (vertical dashed purple line) are the two fitting parameters. (c) An example of the band diagram near a clean Si(100) surface at a negative sample bias. The surface DOS distributions are also plotted at the substrate-vacuum interface with the DOS amplitudes in arbitrary units. The different surface DOS distributions on flat terraces and at the step edge regions will give very different electrostatic characteristics at the surface.

edge were plotted as blue and green colored data points in Figs. 7(a) and 7(b). The band bending data points in red were obtained by substituting E_{PES} with the best-fit energy levels E_1 and E_2 at the SB step edge using the intrinsic edge state model, which will be discussed in the next section. The error bars for each data point represent one standard deviation of the measured peak positions.

Our electrostatic calculations were conducted using a three-dimensional tip-semiconductor tunneling model following Feenstra [80–82]. We assumed a hyperbolic shaped tip [Fig. 6(a)] described by three key parameters, namely, the tip-sample separation (s), tip radius of curvature (R), and the tip potential boundary condition at zero bias (C_{Pot}). It is worth pointing out that in our theoretical calculations, C_{Pot} is defined as the tip potential relative to the ground potential (VBM deep inside the bulk substrate). Since the substrate doping level is experimentally known from SIMS measurements and the commonly used electron affinity energy of Si (4.05 eV) was adopted in this work, the C_{Pot} value depends only on tip work function and is independent of the surface state distributions on the Si surface. The surface dangling bond state distributions on flat terraces were adopted from the photoemission spectroscopy results as described before.

The SB edge effects on the local electrostatic environment are modeled in two different ways. The first model is to treat the edge states as additional extrinsic defect surface states that distribute uniformly over all the surface and the energy space. The measured local band bendings near the SB step edge were used to fit the two edge state parameters, namely, the uniform edge DOS distribution in units of $(\text{cm}^2\,\text{eV})^{-1}$ and an edge state charge neutrality level in units of eV above the VBM at the surface. The edge states below (above) the edge state charge neutrality level are donor (acceptor) -like. The surface charge density was calculated by comparing the Fermi level at the surface with the overall surface charge neutrality level. Surface state resonances with bulk states below the VBM or above the conduction band minimum are not treated in these simulations [82]. A more realistic way is to treat the SB edge states as an intrinsic surface state distribution and therefore the states are localized in specific areas on the surface and in the energy domain. From the STM and STS observations, we limit the observed SB edge states within a 0.8-nm-wide by 6.16-nm-long region that corresponds to an eight-dimer-row–wide SB step edge. The edge state distribution is composed of a pair of occupied and unoccupied state peaks on either side of the Fermi level. The DOS and FWHM at the SB step edge are scaled by the same factors used when scaling the peaks from the flat terraces. SB edge state energy levels E_1 and E_2 are the two fitting parameters in this intrinsic SB edge state model, as listed in the last row in Table I.

In general, we first used the band bending values obtained on flat terraces [blue data points in Figs. 7(a) and 7(b)] as constraints to obtain a set of best-fit tip parameters. We then used these best-fit tip parameters and the observed band bending values at and near the SB step edge [red and green data points in Figs. 7(a) and 7(b)] as constraints to obtain a set of best-fit step edge parameters. Finally, both the best-fit tip and SB edge state parameters were used to quantify the edge

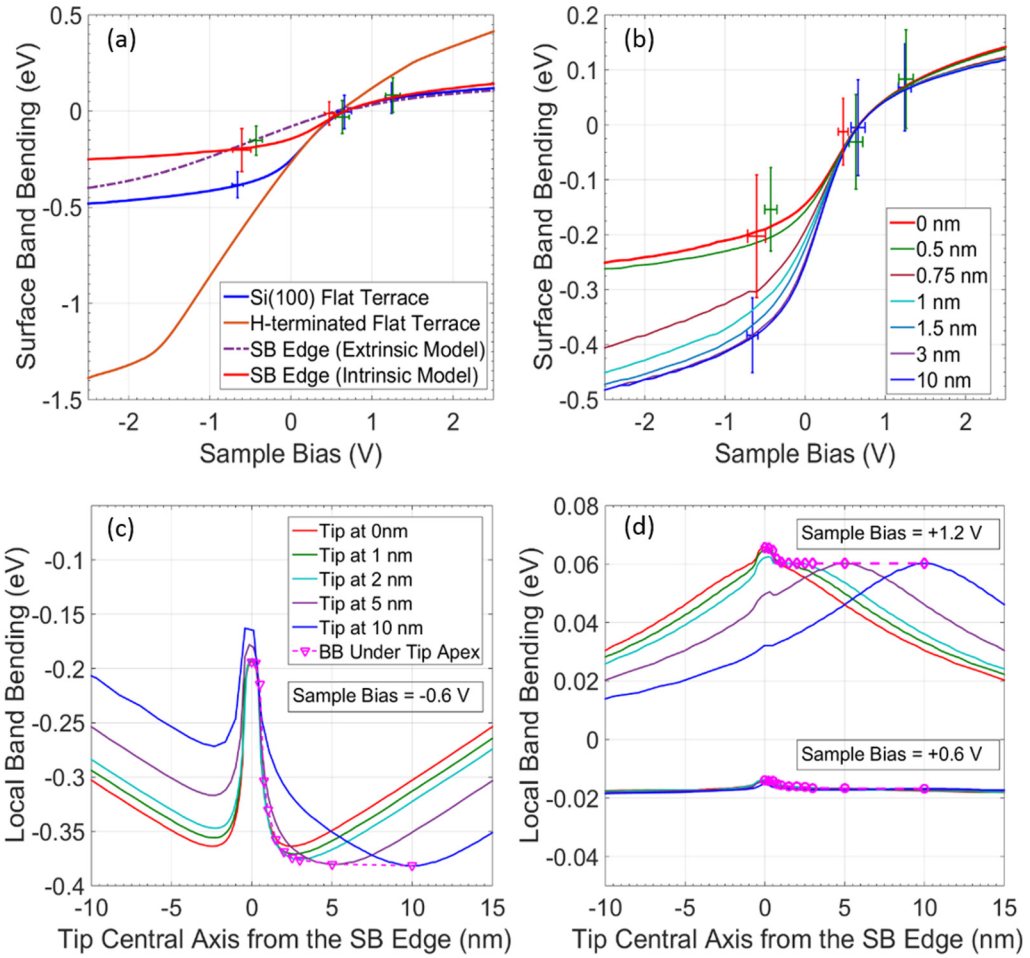

FIG. 7. (a) Simulated band bending curves using the best-fit tip parameters on flat H-terminated Si(100) terraces (solid brown curve), on flat clean Si(100) terraces (solid blue curve), and at the rebonded SB step edge using intrinsic (solid red curve) and extrinsic (dashed purple curve) edge state distribution models. (b) The simulated surface band bending under the tip apex with the tip at different distances from the SB step edge using the intrinsic SB edge state distribution model. According to Eq. (4.1), the experimental band bending data points on flat terraces (blue points), near the SB step edge (green points), and at the SB step edge (red points) are plotted in (a) and (b). Error bars for each point represent one standard deviation of the measured peak positions. (c) The simulated band bending landscapes at -0.6 V sample bias with the tip at different distances from the SB step edge, using the intrinsic edge state model. The band bending landscapes at $+0.6$ V and $+1.2$ V sample biases at the same distances are given in (d). The dashed lines in red-violet connect the local band bending values under the tip apex at different tip positions. These dashed lines are used to map the experimentally observed peak position shift in Fig. 3(c).

induced charge states and their effects on the local electrostatic environment in the STS measurements.

A. Quantifying the tip parameters on flat terraces

The parametric fitting procedures yielded a tip-sample separation of 0.408 nm, a tip radius of curvature of 52 nm, and a C_{Pot} value of -0.608 eV. This predicted large tip radius of curvature is with respect to its local electrostatic potential effects. However, since it is the topmost atom at the tip apex that dominates the tunneling conductance, such a large tip radius does not affect the ability to obtain atomically resolved images and spectroscopy results.

B. Quantifying the edge states using an extrinsic edge state distribution model

Using an extrinsic edge state model, the best-fit effective rebonded SB step edge DOS is $5.3 \times 10^{13}/(\text{cm}^2\,\text{eV})$ with an edge state charge neutrality level approximately 0.01 eV above the VBM. The fitted DOS result is plotted in Fig. 6(b). To properly interpret the best-fit edge parameters in this crude model, one should recall that from the experimental results [Fig. 4(b)] rather than an idealized uniform distribution, the rebonded SB step edge induced states are in fact mainly distributed near the upper edge of the surface band gap. As a result, the fitted charge neutrality level, under the approximation of a uniform edge state distribution, represents a lower limit of the real charge neutrality level of the edge state distribution.

C. Quantifying the edge states using an intrinsic edge state distribution model

Using the intrinsic edge state model, the best-fit edge peak positions for the occupied and unoccupied states at the SB step edge are $E_1 = -0.3782$ eV and $E_2 = +0.4758$ eV above

the VBM. The best-fit SB edge state distribution is plotted in red curves in Fig. 6(b). Figure 7(a) summarizes the simulated surface band bending under the tip apex under different surface conditions.

In Fig. 7(a), the brown curve shows the simulated surface band bending on a flat hydrogen-terminated Si(100) surface, i.e., in the absence of any dangling bond surface state. By adding dangling bond states on the flat terrace, the surface band bending is strongly pinned over the entire sample bias range, as shown by the blue curve. The dashed purple curve shows the calculated band bending under the tip apex in the presence of SB step edges using the best-fit uniform extrinsic edge DOS distribution model. The red curve is the simulated band bending under the tip apex using the best-fit intrinsic edge state distribution model when the tip is at the SB step edge. Comparing the purple and red curves, the extrinsic edge state model gives a stronger pinning effect at small sample biases due to the nonzero SB edge DOS distribution across the Fermi level. But the intrinsic edge state model provides stronger pinning effects at larger sample biases. Figure 7(b) shows the simulated surface band bending under the tip apex with the tip at different distances from the SB step edge using the intrinsic SB edge state distribution model. It can be seen that the SB step edge's influence on the measured band bending under the tip apex becomes negligible when the tip is more than 3 nm away from the SB step edge. This prediction provides a crucial threshold distance within which the LDOS and charge distributions at the rebonded SB step edge are likely to have a significant electrostatic influence on atomically precise quantum structures.

Figures 7(c) and 7(d) show the simulated band bending landscapes with the tip at different distances from the SB step edge under three different sample bias conditions. The dashed curves connect the local band bending values under the tip apex as a function of the tip distance from the SB step edge. At negative sample biases, the local charge arising from the intrinsic SB edge states significantly pin the bands at the SB step edge due to the low-lying unoccupied edge states. At positive sample biases, the local band bending at the SB step edge is slightly enhanced since the occupied edge state lies slightly below the π_2 dangling bond state of the flat terraces. The dashed curves from the simulation agree very well with the observed peak position shifts from Fig. 3(c) as the probe tip moves away from the SB step edge.

D. Characterizing the band gaps at monolayer step edges

We note that, as shown in Fig. 4(b), the surface DOS within the surface band gap and at the Fermi level are nonzero on both the clean and hydrogen-terminated Si(100) surfaces. This nonzero value is the measurement noise level that originates from limited signal-to-noise ratio under the room temperature measurement conditions and from the conductance normalization procedure which exacerbates the tunneling noise at low bias near the Fermi level at the constant tip-sample separation data acquisition conditions. Following Feenstra [40], the onset bias of band extrema on either side of the band gap is determined by assuming a linear onset of the normalized conductance above the noise level. The measured gap on the flat terrace is about 0.5 eV. However, the gap significantly narrows down to about 0.18 eV near and at the rebonded SB step edge. The simulated band bending curves from the intrinsic SB edge states model in Figs. 7(a) and 7(b) were used to correct each of the conductance onset points. Specifically, the band gap values at dimer tTops and dimer troughs on flat terraces and at the SA step edge were corrected by the blue curve in Fig. 7(a). The band gap values at and near the SB step edge were corrected by the red and the red-violet curves in Fig. 7(b). The band gap values before and after band bending corrections are summarized in Table III. The surface band gap value at the SA step edge decreases slightly as compared with the band gap value on flat terraces. The band gap at the SB step edge is only about half of the surface band gap value on flat terraces. Due to the observed band gap narrowing along the rebonded SB step edge, one must use caution when characterizing shallow atomic quantum devices near surfaces or interfaces in the presence of SB step edges. The 1D edge states may introduce additional conducting channels or interband recombination paths having significant impacts on device functionality.

TABLE III. The measured band gaps from the experimental observations and their band bending corrected values from the intrinsic SB edge states model.

Surface regions	Measured band gap (eV)	Band gap as corrected from Band bending simulation (eV)
Dimer top	0.527 ± 0.145	0.324 ± 0.157
Dimer trough	0.540 ± 0.109	0.332 ± 0.117
SA edge	0.473 ± 0.121	0.286 ± 0.122
Near SB edge	0.183 ± 0.046	0.144 ± 0.046
SB edge	0.184 ± 0.045	0.173 ± 0.045

However, one needs to be cautious when interpreting this significant band narrowing behavior at the observed SB step edge. In addition to the atomic orbital hybridization as mentioned previously, the specific finite length of the 1D edge and the substrate doping level are also likely contributions to the LDOS distributions along the step edges.

It is useful to compare the unpaired dangling bond states along the SB step edge as presented in this work with previous studies on 1D dangling bond wire systems on hydrogen-terminated Si(100) surfaces. Interactions among dimers in a dangling bond wire system introduce dispersion from the hybridization of single dangling bond orbitals along the wire, also known as proximity broadening. Theoretical studies by Raza *et al.* [28] on unpaired dangling bond wires of infinite length along the dimer row show a wide surface state band centered near-midgap of about 1.15 eV that eliminates the surface band gap. In contrast, the surface state dispersion of paired dangling bond wires of infinite length shows a semiconducting behavior, very similar to the π and π^* surface state bands on clean Si(100) terraces. Recent density functional theory (DFT) calculations [26,30] studied the energetics and stability of infinite and finite unpaired dangling bond wires. These DFT calculations found that finite unpaired dangling bond wires develop localized electronic states. Hitosugi

et al. [23] observed these localized states created by the finite 1D length using STS on H-terminated Si(100)2 × 1 surfaces.

The effects of substrate doping on the step edge states can be viewed in analogy to charge-induced state shifting [52] observed in isolated individual surface states. Isolated dangling bond states on Si(100) surfaces have been observed by Boland [25] and Hitosugi *et al.* [23] on moderately doped *p*-type substrates and heavily doped *n*-type substrates, where two peaks with similar magnitude are introduced on each side of the surface Fermi level. From the observations of Reusch *et al.* [52], heavily doped *p*-type substrates give rise to a prominent unpaired dangling bond state peak above the Fermi level at the lower edge of the π^* band, but no additional occupied states above the π band. Observation of the dangling bond features across the SB step edge on the heavily boron-doped *p*-type substrate, shown in Fig. 4(b), shows a prominent unoccupied edge state peak above the Fermi level and a small DOS enhancement below the Fermi level, similar to the isolated unpaired dangling bonds on heavily doped *p*-type substrates.

V. CONCLUSION

We have conducted a detailed spatially resolved scanning tunneling spectroscopy study across monolayer step edges on Si(100) surfaces, and quantitatively determined the local density of state distributions and band gap information at the step edges. The influence on the local electrostatic environment due to step edge states has been quantified while accounting for the effects of scanning tunneling measurement conditions. The dangling bond states on Si(100) surfaces have been utilized as a fingerprint to quantify the local band bending landscape and to make corrections to the experimentally observed surface state energy levels and band gap values at the step edge regions. We observe a significant band gap narrowing behavior along a rebonded SB step edge on a degenerately boron-doped *p*-type Si substrate. This study provides a clear experimental demonstration and theoretical elucidation of the local electronic environment near the monolayer step edges on Si(100) surfaces, which paves the way towards successful *in situ* relocation and characterization of dopant quantum structures for future silicon quantum computing [9].

ACKNOWLEDGMENTS

This work was sponsored by the Innovations in Measurement Science (IMS) project at NIST: Single atom transistors to solid states quantum computing. The authors wish to thank Jonathan Wyrick, Randall Feenstra, Theodore L. Einstein, and Ian Appelbaum for useful conversations.

[1] M. Fuechsle, S. Mahapatra, F. A. Zwanenburg, M. Friesen, M. A. Eriksson, and M. Y. Simmons, Nat. Nanotechnol. **5**, 502 (2010).
[2] M. Fuechsle, J. A. Miwa, S. Mahapatra, H. Ryu, S. Lee, O. Warschkow, L. C. L. Hollenberg, G. Klimeck, and M. Y. Simmons, Nat. Nanotechnol. **7**, 242 (2012).
[3] P. Bogusławski, Q. M. Zhang, Z. Zhang, and J. Bernholc, Phys. Rev. Lett. **72**, 3694 (1994).
[4] J.-Y. Koo, J.-Y. Yi, C. Hwang, D.-H. Kim, G. Lee, and S. Lee, Phys. Rev. B **57**, 8782 (1998).
[5] X. Deng, P. Namboodiri, K. Li, X. Wang, G. Stan, A. F. Myers, X. Cheng, T. Li, and R. Silver, Appl. Surf. Sci. **378**, 301 (2016).
[6] K. Li, N. Pradeep, S. Chikkamaranahalli, G. Stan, R. Attota, J. Fu, and R. Silver, J. Vac. Sci. Technol. B **29**, 041806 (2011).
[7] B. S. Swartzentruber, Phys. Rev. B **55**, 1322 (1997).
[8] S. Goswami, K. A. Slinker, M. Friesen, L. M. McGuire, J. L. Truitt, C. Tahan, L. J. Klein, J. O. Chu, P. M. Mooney, D. W. van der Weide, R. Joynt, S. N. Coppersmith, and M. A. Eriksson, Nat. Phys. **3**, 41 (2007).
[9] T. D. Ladd, J. R. Goldman, F. Yamaguchi, Y. Yamamoto, E. Abe, and K. M. Itoh, Phys. Rev. Lett. **89**, 017901 (2002).
[10] S. C. Erwin and F. J. Himpsel, Nat. Commun. **1**, 58 (2010).
[11] J. E. Griffith, G. P. Kochanski, J. A. Kubby, and P. E. Wierenga, J. Vac. Sci. Technol. A **7**, 1914 (1989).
[12] J. E. Griffith, J. A. Kubby, P. E. Wierenga, R. S. Becker, and J. S. Vickers, J. Vac. Sci. Technol. A **6**, 493 (1988).
[13] R. J. Hamers, R. M. Tromp, and J. E. Demuth, Phys. Rev. B **34**, 5343 (1986).
[14] H. Tochihara, T. Sato, T. Sueyoshi, T. Amakusa, and M. Iwatsuki, Phys. Rev. B **53**, 7863 (1996).
[15] T. Yamaguchi and N. Fujima, Surf. Sci. **242**, 233 (1991).
[16] R. A. Wolkow, Phys. Rev. Lett. **68**, 2636 (1992).
[17] J. J. de Miguel, C. E. Aumann, R. Kariotis, and M. G. Lagally, Phys. Rev. Lett. **67**, 2830 (1991).
[18] O. L. Alerhand, A. N. Berker, J. D. Joannopoulos, D. Vanderbilt, R. J. Hamers, and J. E. Demuth, Phys. Rev. Lett. **64**, 2406 (1990).
[19] P. Bedrossian and E. Kaxiras, Phys. Rev. Lett. **70**, 2589 (1993).
[20] C. Pearson, M. Krueger, R. Curtis, B. Borovsky, X. Shi, and E. Ganz, J. Vac. Sci. Technol. A **13**, 1506 (1995).
[21] J.-Y. Koo, J.-Y. Yi, C. Hwang, D.-H. Kim, S. Lee, and J. Cho, Phys. Rev. B **54**, 10308 (1996).
[22] T. Komura, M. Yoshimura, and T. Yao, J. Vac. Sci. Technol. B **14**, 906 (1996).
[23] T. Hitosugi, T. Hashizume, S. Heike, S. Watanabe, Y. Wada, T. Hasegawa, and K. Kitazawa, Jpn. J. Appl. Phys. **36**, L361 (1997).
[24] W. Ye, K. Min, P. P. Martin, A. A. Rockett, N. R. Aluru, and J. W. Lyding, Surf. Sci. **609**, 147 (2013).
[25] J. J. Boland, Phys. Rev. Lett. **67**, 2591 (1991).
[26] R. Robles, M. Kepenekian, S. Monturet, C. Joachim, and N. Lorente, J. Phys.: Condens. Matter **24**, 445004 (2012).
[27] S. Watanabe, Y. A. Ono, T. Hashizume, and Y. Wada, Phys. Rev. B **54**, R17308 (1996).
[28] H. Raza, Phys. Rev. B **76**, 045308 (2007).
[29] J.-H. Cho and L. Kleinman, Phys. Rev. B **66**, 235405 (2002).
[30] J.-H. Lee and J.-H. Cho, Surf. Sci. **605**, L13 (2011).
[31] D. R. Bowler, J. Phys.: Condens. Matter **16**, R721 (2004).
[32] H. Kawai, F. Ample, Q. Wang, Y. K. Yeo, M. Saeys, and C. Joachim, J. Phys.: Condens. Matter **24**, 095011 (2012).
[33] V. A. Ukraintsev, Z. Dohnálek, and J. T. Yates, Jr., Surf. Sci. **388**, 132 (1997).

[34] R. Boguslawski, Q. M. Zhang, Z. Zhang, C. Roland, and J. Bernholc, Mater. Sci. Eng., B **30**, 167 (1995).
[35] R. Fischer, N. Chand, W. Kopp, H. Morkoc, L. P. Erickson, and R. Youngman, Appl. Phys. Lett. **47**, 397 (1985).
[36] D. Saloner, J. A. Martin, M. C. Tringides, D. E. Savage, C. E. Aumann, and M. G. Lagally, J. Appl. Phys. **61**, 2884 (1987).
[37] S. Tsunenori and H. Gen, Jpn. J. Appl. Phys. **25**, L78 (1986).
[38] D. J. Chadi, Phys. Rev. Lett. **59**, 1691 (1987).
[39] B. S. Swartzentruber, Y. W. Mo, M. B. Webb, and M. G. Lagally, J. Vac. Sci. Technol. A **7**, 2901 (1989).
[40] R. M. Feenstra, Phys. Rev. B **50**, 4561 (1994).
[41] R. M. Feenstra, J. A. Stroscio, and A. P. Fein, Surf. Sci. **181**, 295 (1987).
[42] Y. Enta, S. Suzuki, and S. Kono, Phys. Rev. Lett. **65**, 2704 (1990).
[43] L. S. O. Johansson, P. E. S. Persson, U. O. Karlsson, and R. I. G. Uhrberg, Phys. Rev. B **42**, 8991 (1990).
[44] L. S. O. Johansson and B. Reihl, Surf. Sci. **269**, 810 (1992).
[45] P. E. J. Eriksson, M. Adell, K. Sakamoto, and R. I. G. Uhrberg, Phys. Rev. B **77**, 085406 (2008).
[46] T. Wakita, H. Okazaki, Y. Takano, M. Hirai, Y. Muraoka, and T. Yokoya, Physica C (Amsterdam, Neth.) **470** (Supplement 1) S641 (2010).
[47] L. S. O. Johansson, R. I. G. Uhrberg, P. Mårtensson, and G. V. Hansson, Phys. Rev. B **42**, 1305 (1990).
[48] J. E. Ortega and F. J. Himpsel, Phys. Rev. B **47**, 2130 (1993).
[49] C. Kentsch, M. Kutschera, M. Weinelt, T. Fauster, and M. Rohlfing, Phys. Rev. B **65**, 035323 (2001).
[50] T. Fauster, S. Tanaka, and K. Tanimura, Phys. Rev. B **84**, 235444 (2011).
[51] K. S. Nakayama, M. M. G. Alemany, T. Sugano, K. Ohmori, H. Kwak, J. R. Chelikowsky, and J. H. Weaver, Phys. Rev. B **73**, 035330 (2006).
[52] T. C. G. Reusch, O. Warschkow, M. W. Radny, P. V. Smith, N. A. Marks, N. J. Curson, D. R. Mckenzie, and M. Y. Simmons, Surf. Sci. **601**, 4036 (2007).
[53] M. Rohlfing, P. Krüger, and J. Pollmann, Phys. Rev. B **52**, 1905 (1995).
[54] R. Asahi, W. Mannstadt, and A. J. Freeman, Phys. Rev. B **62**, 2552 (2000).
[55] D. J. Chadi, Phys. Rev. Lett. **43**, 43 (1979).
[56] J. E. Northrup, Phys. Rev. B **47**, 10032 (1993).
[57] H. Okada, Y. Fujimoto, K. Endo, K. Hirose, and Y. Mori, Phys. Rev. B **63**, 195324 (2001).
[58] H. Kageshima and M. Tsukada, Phys. Rev. B **46**, 6928 (1992).
[59] F. J. Himpsel and D. E. Eastman, J. Vac. Sci. Technol. **16**, 1297 (1979).
[60] K. Hata, Y. Shibata, and H. Shigekawa, Phys. Rev. B **64**, 235310 (2001).
[61] X. R. Qin and M. G. Lagally, Phys. Rev. B **59**, 7293 (1999).
[62] T. Yokoyama and K. Takayanagi, Phys. Rev. B **57**, R4226 (1998).
[63] M. Dubois, L. Perdigão, C. Delerue, G. Allan, B. Grandidier, D. Deresmes, and D. Stiévenard, Phys. Rev. B **71**, 165322 (2005).
[64] K. Hata, S. Ozawa, and H. Shigekawa, Surf. Sci. **441**, 140 (1999).
[65] P. Avouris and R. Wolkow, Phys. Rev. B **39**, 5091 (1989).
[66] T. Tabata, T. Aruga, and Y. Murata, Surf. Sci. **179**, L63 (1987).
[67] M. T. Yin and M. L. Cohen, Phys. Rev. B **24**, 2303 (1981).
[68] J. J. Boland, Phys. Rev. Lett. **67**, 1539 (1991).
[69] X. R. Qin, B. S. Swartzentruber, and M. G. Lagally, Phys. Rev. Lett. **84**, 4645 (2000).
[70] S. G. Jaloviar, J.-L. Lin, F. Liu, V. Zielasek, L. McCaughan, and M. G. Lagally, Phys. Rev. Lett. **82**, 791 (1999).
[71] T. Sato, T. Sueyoshi, T. Amakusa, M. Iwatsuki, and H. Tochihara, Surf. Sci. **340**, 328 (1995).
[72] T. Komura, T. Yao, and M. Yoshimura, Phys. Rev. B **56**, 3579 (1997).
[73] S. Jeong and A. Oshiyama, Phys. Rev. Lett. **81**, 5366 (1998).
[74] R. E. Butera, D. A. Mirabella, C. M. Aldao, and J. H. Weaver, Phys. Rev. B **82**, 045309 (2010).
[75] A. Laracuente and L. J. Whitman, Surf. Sci. **476**, L247 (2001).
[76] P. E. J. Eriksson and R. I. G. Uhrberg, Phys. Rev. B **81**, 125443 (2010).
[77] H. Koh, J. W. Kim, W. H. Choi, and H. W. Yeom, Phys. Rev. B **67**, 073306 (2003).
[78] E. Landemark, C. J. Karlsson, Y. C. Chao, and R. I. G. Uhrberg, Phys. Rev. Lett. **69**, 1588 (1992).
[79] M. V. Gomoyunova and I. I. Pronin, Tech. Phys. **49**, 1249 (2004).
[80] R. M. Feenstra, J. Vac. Sci. Technol. B **21**, 2080 (2003).
[81] R. M. Feenstra, Y. Dong, M. P. Semtsiv, and W. T. Masselink, Nanotechnology **18**, 044015 (2007).
[82] R. M. Feenstra, S. Gaan, G. Meyer, and K. H. Rieder, Phys. Rev. B **71**, 125316 (2005).